





# Time-dependent diffusivity and kurtosis in phantoms and patients with head and neck cancer

Eddy Solomon<sup>1</sup>  | Gregory Lemberskiy<sup>2</sup>  | Steven Baete<sup>2</sup> | Kenneth Hu<sup>3</sup> |  
Dariya Malyarenko<sup>4</sup> | Scott Swanson<sup>4</sup> | Amita Shukla-Dave<sup>5</sup> |  
Stephen E. Russek<sup>6</sup>  | Elcin Zan<sup>2</sup> | Sungheon Gene Kim<sup>1</sup> 

<sup>1</sup>Department of Radiology, MRI Research Institute, Weill Cornell Medical College, New York, New York, USA

<sup>2</sup>Department of Radiology, New York University, New York, New York, USA

<sup>3</sup>Department of Radiation Oncology, New York University, New York, New York, USA

<sup>4</sup>Department of Radiology, Michigan Medicine, University of Michigan, Ann Arbor, Michigan, USA

<sup>5</sup>Departments of Medical Physics and Radiology, Memorial Sloan Kettering Cancer Center, New York, New York, USA

<sup>6</sup>National Institute of Standards and Technology, Boulder, Colorado, USA

## Correspondence

Eddy Solomon, Department of Radiology at Weill Cornell Medicine, Cornell University, 407 E. 61st Street, New York, NY 10065, USA.

Email: [eds4001@med.cornell.edu](mailto:eds4001@med.cornell.edu)

## Funding information

National Institutes of Health, Grant/Award Numbers: R01CA160620, R01CA219964, R01EB028774, UH3CA228699

**Purpose:** To assess the reliability of measuring diffusivity, diffusional kurtosis, and cellular-interstitial water exchange time with long diffusion times (100–800 ms) using stimulated-echo DWI.

**Methods:** Time-dependent diffusion MRI was tested on two well-established diffusion phantoms and in 5 patients with head and neck cancer. Measurements were conducted using an in-house diffusion-weighted STEAM-EPI pulse sequence with multiple diffusion times at a fixed TE on three scanners. We used the weighted linear least-squares fit method to estimate time-dependent diffusivity,  $D(t)$ , and diffusional kurtosis,  $K(t)$ . Additionally, the Kärger model was used to estimate cellular-interstitial water exchange time ( $\tau_{ex}$ ) from  $K(t)$ .

**Results:** Diffusivity measured by time-dependent STEAM-EPI measurements and commercial SE-EPI showed comparable results with  $R^2$  above 0.98 and overall  $5.4 \pm 3.0\%$  deviation across diffusion times. Diffusional kurtosis phantom data showed expected patterns: constant  $D$  and  $K = 0$  for negative controls and slow varying  $D$  and  $K$  for samples made of nanoscopic vesicles. Time-dependent diffusion MRI in patients with head and neck cancer found that the Kärger model could be considered valid in  $72\% \pm 23\%$  of the voxels in the metastatic lymph nodes. The median cellular-interstitial water exchange time estimated for lesions was between 58.5 ms and 70.6 ms.

**Conclusions:** Based on two well-established diffusion phantoms, we found that time-dependent diffusion MRI measurements can provide stable diffusion and kurtosis values over a wide range of diffusion times and across multiple MRI systems. Moreover, estimation of cellular-interstitial water exchange time can be achieved using the Kärger model for the metastatic lymph nodes in patients with head and neck cancer.

## KEYWORDS

diffusion phantom, Kärger model, kurtosis, STEAM EPI

## 1 | INTRODUCTION

Diffusion MRI (dMRI) has become the modality of choice to assess the cellular properties of tumors, as the diffusion of water molecules is highly sensitive to tissue microstructure.<sup>1–3</sup> While dMRI signal is sensitive to different biophysical properties of tissue, such as cell size and density, quantitative assessment of those microstructural properties remains challenging. Among these microstructural properties are the presence of barriers (eg, cell membranes), cellular compartments (eg, intracellular and extracellular spaces), and various cellular organelles. Diffusivity is typically interpreted as a measure of cell density and extracellular water fraction.<sup>4</sup> Consistent with this interpretation, dMRI of malignant tumors typically showed a decrease in diffusivity,<sup>5,6</sup> which was correlated with increased cell density measured by histology<sup>7</sup> and thus a decrease in extracellular space. However, the diffusivity derived from dMRI acquisition is not a constant for a given biological tissue, but a function of measurement conditions, such as diffusion-weighting strength and the diffusion time.<sup>8–12</sup> Hence, it is crucial to consider both factors carefully when planning dMRI experiments.

It is even more important to consider the dependency of dMRI-derived parameters on diffusion time when a higher-order term of diffusion signal, such as diffusional kurtosis, is included with a stronger diffusion weighting. Quantifying the degree of deviation from Gaussian diffusion can be useful in characterizing the associated tissue structures. For this purpose, diffusional kurtosis imaging (DKI) provides a practical clinical technique to probe the microscopic structure of biologic tissues.<sup>13</sup> It has been demonstrated that diffusional kurtosis is a more specific measure of tissue structure, such as cellular compartments and membranes, than diffusivity.<sup>14,15</sup> It was also shown that diffusional kurtosis has greater sensitivity and specificity than diffusivity for assessment of hepatocellular carcinoma viability after treatment<sup>16</sup> and as a marker to assess cell viability to evaluate early treatment response.<sup>17</sup> However, the variability of diffusion kurtosis parameters as a function of diffusion time is still not fully understood.

Diffusional kurtosis increases with the diffusion time when the cellular barriers are impermeable, as in the white matter.<sup>18</sup> When the diffusion time is long enough and the tissue contains permeable barriers, the diffusional kurtosis monotonically decreases as diffusion time increases.<sup>19</sup> These study results support that it is important to report the diffusion time used for a diffusional kurtosis measurement. More importantly, these studies show that by using two-compartment modeling, the time-dependent diffusional kurtosis can be used to measure the cellular-interstitial water exchange time.<sup>14,19,20</sup>

Cellular-interstitial water exchange time ( $\tau_{\text{ex}}$ ) has been suggested as a marker of cellular metabolism.<sup>21</sup> The value of  $\tau_{\text{ex}}$  can be used to assess the increased metabolic activity associated with cancer<sup>22</sup> and the metastatic potential that could be associated with long term survival as shown for head and neck cancer.<sup>23</sup> Diffusion kurtosis imaging parameters  $D$ ,  $K$ , and  $\tau_{\text{ex}}$  can be useful imaging biomarkers for monitoring both cellular viability and metabolism. Based on former Monte Carlo simulations<sup>19</sup> and breast cancer measurements,<sup>20</sup> the water exchange time in cancer cells is expected to be about 100 ms. Thus, to measure the cellular-interstitial water exchange time, it is necessary to conduct a series of DKI scans with multiple diffusion times longer than 100 ms. However, conventional spin echo-based DWI pulse sequences are not adequate for this purpose, due to the increased TE to accommodate a long diffusion time. Instead, stimulated echo acquisition mode (STEAM)-DWI pulse sequences have been adopted to achieve long diffusion time without the need to increase the TE.<sup>8,20,24</sup> Nevertheless, the evaluation of STEAM-based imaging for diffusion kurtosis has not been conducted with commercially available clinical scanners for a range of diffusional kurtosis values expected for cancer.

The purpose of this study is to investigate how reliably diffusivity and diffusional kurtosis can be measured for long diffusion times (100–800 ms) using STEAM DWI. We used two well-established diffusion phantoms: one from the National Institute of Standards and Technology (NIST) and another from the University of Michigan in collaboration with the Quantitative Imaging Network (QIN) of the National Cancer Institute (NCI). The same pulse sequence was also tested to measure diffusion parameters and cellular-interstitial water exchange time in patients with head and neck cancer.

## 2 | METHODS

### 2.1 | Theory

The diffusion MRI signal can be expressed as the cumulant expansion, as follows<sup>14</sup>:

$$\ln[S(b)] = \ln(S_0) - bD + \frac{1}{6}b^2D^2K + O(b^3) \quad (1)$$

where  $S(b)$  and  $S_0$  are the signal intensities with and without diffusion weighting;  $D$  denotes diffusivity;  $K$  denotes diffusional kurtosis; and  $O(b^3)$  is the approximation error. The diffusion weighting, also known as  $b$ -value, is defined as a single parameter,  $b = q^2t$ , where  $q$  is defined as the accumulated diffusion gradient strength during the gradient pulse duration  $\delta$ :  $q = \int_0^\delta g(t') dt'$ , and  $t$  is defined as

the diffusion time (also typically known as  $\Delta$ ). The signal equation in Eq. 1 is constrained by a maximum  $b$ -value<sup>10</sup>:  $b_{\max} < 3/(DK)$ . When a voxel has multiple Gaussian compartments with impermeable barriers (ie, no water exchange),  $K$  is given by the relative variance of compartmental diffusivities,  $K = 3 \frac{\text{var}(D)}{D^2}$ . In the absence of microscopic structures, the variance of diffusivity is zero such that  $K = 0$ , which is the case of simple Gaussian diffusion.

A non-Gaussian diffusion environment can be characterized by a nonzero kurtosis term  $K$  and the time dependence of all the cumulants, such as  $D(t)$  and  $K(t)$ .<sup>25</sup> In this case, tissue complexity can be probed in two complementary approaches: (i) by quantifying higher-order cumulants at a given diffusion time (ie, by increasing the  $b$ -value at fixed  $t$ ) or by (ii) probing the time dependence of the cumulants by varying the diffusion time  $t$ . For both approaches, biophysical modeling of the diffusional tissue microenvironment is required.

The diffusion time dependence of the cumulants is affected by both the time for water molecules to travel between the barriers and the permeability of the barriers. When the permeability is not known, it is helpful to consider the diffusion time dependence with respect to  $t_c$ , the characteristic time for restrictive effects determined by a typical time to diffuse between cell membranes, as  $t_c$  would be the lower limit of  $\tau_{\text{ex}}$ . In the barrier-limited exchange case  $t_c \ll \tau_{\text{ex}}$ , it has been shown that  $K(t)$  peaks at about  $t \sim t_c$ .<sup>19</sup> For short diffusion times  $t \ll t_c$ , the increase of the kurtosis with diffusion time can be viewed as resulting from the restriction of water molecules by membranes. For long diffusion times  $t \gg t_c$ , as measured in this study ( $\geq 100$  ms), both intracellular and extracellular compartments are coarse-grained by diffusion (ie, long-time diffusion regime),<sup>26</sup> and the overall diffusivity  $D(t)$  becomes constant and behaves like a Gaussian diffusion, as predicted by the Kärger model (KM).<sup>27</sup> The KM assumes that a tissue has two molecular spin-carrying pools (intracellular and extracellular) with Gaussian diffusion, each characterized by diffusion coefficients ( $D_i$  and  $D_e$ ), fractions  $v_i$  and  $v_e$ , and mean lifetime in individual compartments (residence times)  $\tau_i$  and  $\tau_e$ , respectively. The value of  $t_c$  is related to the characteristic diffusion times of the extracellular and intracellular compartments,  $t_{D,e}$  and  $t_{D,i}$ :  $t_c = \max\{t_{D,e}, t_{D,i}\}$  and  $t_c \ll \tau_i$  and  $\tau_e$ .<sup>19</sup> Following KM,  $D$  is constant when  $t \gg t_c$ :

$$D = (1 - v_e)D_e + v_e D_i = \text{const.} \quad (2)$$

The value of  $K(t)$  can be described as a function of the exchange time  $\tau_{\text{ex}} = v_i \tau_e = v_e \tau_i$ :

$$K(t) = K_\infty + K_0 \frac{2\tau_{\text{ex}}}{t} \left[ 1 - \frac{\tau_{\text{ex}}}{t} \left( 1 - e^{-t/\tau_{\text{ex}}} \right) \right] \quad (3)$$

where  $K_0 + K_\infty$  is the maximum of  $K$  in the case of impermeable barriers, and  $K_\infty$  accounts for a partial volume effect of any tissue compartment not involved in water exchange. A Monte Carlo numerical simulation study<sup>19</sup> showed that KM is a valid model when  $t \gg t_c$ ; thus, the exchange time  $\tau_{\text{ex}}$  can be measured from  $K(t)$  using Eq. 3. This was previously demonstrated with mouse tumor models.<sup>20</sup> Furthermore, the time dependence of the cumulants  $D$  and  $K(t)$  in Eqs. 2 and 3 can be used to estimate diffusion-weighted signals as follows:

$$S_e(t, b) = S_{e0}(t) \exp \left( -bD + \frac{1}{6} b^2 D^2 K(t) \right). \quad (4)$$

The estimated signal  $S_e(t, b)$  can be linearly scaled by adjusting  $S_{e0}(t)$  to match the measured signal  $S_m(t, b)$  for each diffusion time. Then, estimation of four KM parameters is conducted by minimizing the sum of squared differences between the estimated and measured signals for each voxel:

$$\{K_0, K_\infty, \tau_{\text{ex}}, D\} = \arg \min_{t,b} \sum (S_e(t, b) - S_m(t, b))^2 \quad (5)$$

where the upper  $b$ -value limit ( $b < 3/(DK)$ ) is applied per diffusion time.

## 2.2 | Time-dependent diffusion experiments

Time-dependent diffusion experiments were performed using a STEAM pulse sequence. An in-house STEAM pulse sequence (Figure 1) has been developed based on a conventional EPI acquisition (STEAM EPI). The sequence calculates the total diffusion weighting from all the gradients for a given diffusion time (ie,  $t = \Delta$ ) and adjusts the diffusion-weighted gradients ( $G_d$ ) in accordance with the desired  $b$ -value. To avoid potential directional bias along the three orthogonal directions, the strength of the gradient for each direction and diffusion time was adjusted in order to achieve the same  $b$ -value for all three directions. The value of  $G_d$  was kept lower than 70 mT/m in all of our scans. Flexible diffusion times were manually set by varying the mixing time while keeping other key diffusion and imaging parameters constant, such as  $b$ -value and TE. In our study, diffusion times were varied from 100 ms to 800 ms, and  $b$ -values were held constant.

## 2.3 | Diffusion phantom

We tested the time-dependent dMRI on two diffusion phantoms. The first phantom<sup>28</sup> was a diffusion phantom

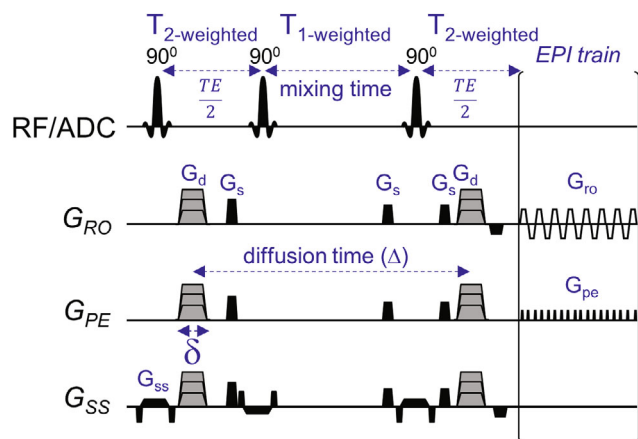


**FIGURE 1** Time-dependent diffusion and kurtosis experiments using STEAM EPI. This in-house STEAM EPI sequence allows to use a flexible range of long diffusion times by extending the mixing time. In this study, diffusion times ranging from 100 ms and above were used while keeping TE and  $b$ -values constant by adjusting the diffusion weighting gradients ( $G_d$ ) accordingly. Diffusion gradients indicated by stepped gray gradients are separated by a diffusion time  $\Delta$ . Refocusing echo with  $\frac{TE}{2}$  delay is placed symmetrically after the excitation pulse and before acquisition. Spoiler gradients  $G_s$  rotate with the diffusion gradients. Abbreviations:  $G_d$ , diffusion-weighting gradients;  $G_{pe}$ , phase-encode gradients;  $G_{ro}$ , readout gradient;  $G_s$ , spoiler gradients;  $G_{ss}$ , slice-selective gradient

provided by and was tested on three MAGNETOM MRI 3T systems (Siemens Healthcare) at two imaging centers using a 20-channel head coil array. A Prisma scanner at New York University was designated as “Site1,” and Prisma and Skyra scanners at Weill Cornell Medicine were designated as “Site2” and “Site3,” respectively. The NIST phantom is a well-established tool for assessing measurement of isotropic water Gaussian diffusion coefficients. This phantom contains thirteen 30-ml vials with different polyvinylpyrrolidone (PVP) concentrations (0%, 10%, 20%, 30%, 40%, and 50%), bathed in ice water, to keep the temperature of the phantom close to 0°C. To minimize temperature variance across sites, while preparing the phantom ice-water bath, we performed temperature measurements using a digital temperature probe until the temperature inside the phantom reached 0°C.

This phantom was used to test the reproducibility of measuring diffusivity over different diffusion times using our in-house STEAM-EPI pulse sequence. The imaging parameters for the STEAM-EPI sequence were TR/TE = 6000/56 ms,  $1.6 \times 1.6 \times 5.0$  mm<sup>3</sup> resolution, bandwidth = 1200 Hz/pixel, and six slices acquired in coronal orientation with fat suppression. The STEAM-EPI diffusion parameters included  $\delta = 8$  ms with five diffusion times ( $\Delta = 200, 400, 600, 700,$  and  $800$  ms), one  $b = 0$ , and five  $b$ -shells ( $b = 200, 600, 1000, 1600,$  and  $2000$  s/mm<sup>2</sup>) with three diffusion directions along

the  $x$ ,  $y$ , and  $z$  axes. For the diffusion times, the mixing times were 186, 386, 586, 686, and 786 ms. The scan time of STEAM EPI for one diffusion time was 1:54 min. For comparison, the standard vendor-provided spin-echo EPI (SE-EPI) sequence was run with the following imaging parameters: TR/TE = 10 000/101 ms,  $0.5 \times 0.5 \times 4.0$  mm<sup>3</sup> resolution, with fat suppression, bandwidth = 1184 Hz/pixel, and 25 slices acquired in coronal orientation. The SE-EPI was used with a bipolar twice-refocused scheme ( $\Delta \sim TE/2 = 50$  ms, three  $b$ -shells [ $b = 500, 900, 2000$  s/mm<sup>2</sup>], and scan time = 2:12 min).

## 2.4 | Diffusional kurtosis imaging phantom

A DKI phantom<sup>29</sup> developed at the University of Michigan was provided as part of a collaboration with the Quantitative Imaging Network at the National Cancer Institute. This phantom was tested on a Prisma 3T system at Weill Cornell Medicine. The kurtosis phantom samples were made from cetearyl alcohol, behentrimethyl ammonium chloride, stearylamidopropyl dimethylamine, and cetyltrimethyl ammonium bromide. Each sample has a unique identification (ID), where “C” indicates a mixture of cetearyl alcohol and cetyltrimethyl ammonium bromide with an alcohol-to-surfactant molar ratio of 3:1 or 5:1 (labeled in the beginning of the sample ID), and “CSB” indicates a mixture of cetearyl alcohol, behentrimethyl ammonium chloride, and stearylamidopropyl dimethylamine in a ratio of 7:1:1. The %(wt/wt) solid-in-water ranges between 0.5% and 2.5%, as indicated by the number at the end of the sample ID. To simplify, in the legend of Figure 3, each sample ID was also numbered (DK#), while the sample ID mapping is provided in brackets. Additionally, the phantom includes two negative controls ( $K = 0$ ) of 20% and 40% PVP solutions in water, designated as PVP20 and PVP40, respectively.

The kurtosis phantom was used for evaluation of the diffusivity and kurtosis values measured by our STEAM-EPI sequence. The imaging parameters were identical to the ones used for the NIST phantom. The scans were performed at room temperature between 20°C and 21°C. The STEAM-EPI diffusion parameters included  $\delta = 10$  ms with six diffusion times ( $\Delta = 110, 200, 400, 600, 700,$  and  $800$  ms), one  $b = 0$ , and 10  $b$ -shells ( $b = 70, 80, 100, 200, 500, 800, 1000, 1500, 2000,$  and  $2500$  s/mm<sup>2</sup>) with three diffusion directions along the  $x$ ,  $y$ , and  $z$  axes. For varying diffusion time, the mixing times were 86, 186, 386, 586, 686, and 786 ms. The scan time of STEAM EPI for one diffusion time was 3:24 min. The conventional SE-EPI sequence included the following imaging parameters: TR/TE = 5000/91 ms,  $1.6 \times 1.6 \times 5.0$  mm<sup>3</sup> resolution,

with fat suppression, bandwidth = 1202 Hz/pixel, and six slices acquired in coronal orientation. For the Kurtosis phantom, SE-EPI was used with a bipolar twice-refocused scheme ( $\Delta \sim TE/2 = 45$  ms, nine  $b$ -shells [ $b = 50, 100, 200, 500, 800, 1000, 1500, 2000, \text{ and } 2500$  s/mm<sup>2</sup>], and scan time = 2:52 min).

## 2.5 | Head and neck cancer patient study

Five patients with tonsil biopsy-proven oropharyngeal squamous cell carcinoma with metastatic lymph nodes were recruited for measurement of dMRI with long diffusion times. This Health Insurance Portability and Accountability Act-compliant prospective study was performed with approval from our institutional review board, and written informed consent was obtained from all subjects. All data were acquired with our STEAM-EPI sequence on a 3T MAGNETOM Prisma MRI system using a 20-channel head/neck coil array. The STEAM-EPI imaging parameters included TR/TE = 5000/60 ms, resolution =  $1.5 \times 1.5 \times 4.0$  mm<sup>3</sup>, FOV = 190 mm, partial Fourier 6/8, and GRAPPA with  $R = 2$ . The STEAM-EPI diffusion parameters included  $\delta = 15$  ms with five diffusion times ( $\Delta = 100, 200, 300, 500, \text{ and } 700$  ms), one  $b = 0$  and four  $b$ -shells ( $b = 200, 1000, 2000, \text{ and } 3000$  s/mm<sup>2</sup>) with three diffusion directions along the  $x, y, \text{ and } z$  axes. For the varying diffusion time, the mixing time was 80, 180, 280, 480, and 680 ms. The scan time for one diffusion time was 1:54 min. To avoid the intravoxel incoherent motion (IVIM) effect,  $b_0$  data were not included in the final analysis.

## 2.6 | Diffusion MRI data analysis

Each set of images was denoised<sup>30</sup> and de-Gibbsed.<sup>31</sup> The estimated noise level<sup>32</sup> was then used to correct the signal for Rician bias. Data were also corrected for eddy currents and off-resonance effects using FSL package.<sup>33</sup> To further correct for motion effects in the patient scans, each data set was registered to a reference  $b_0$  image by a rigid image registration function (*MATLAB* “imregtform” function; MathWorks) over all  $b$ -values and diffusion times. Additionally, nonlocal means filtering was applied on the final images.<sup>34</sup> Following postprocessing, diffusion and kurtosis maps were generated via a weighted linear least-square fit method.<sup>35</sup> The KM was used for estimating  $K_0, K_\infty, D, \text{ and } \tau_{\text{ex}}$  for each voxel by minimization function (*MATLAB* “fminsearch” function). To minimize Eq. 5, we chose a set of 100 initial random values between  $K_0 = [0 \ 1], K_\infty = [0 \ 1], D = [0 \ 2], \text{ and } \tau_{\text{ex}} = [10 \ 100]$ . Moreover, the final estimates were selected only if (a) minimization function successfully converged to a solution and (b) fit values and

their objective function values were above zero. The final KM estimates were the median over these values. To test the assumption that the median value indeed reflects a good estimate of the solution, Figure S1 shows an example of how each parameter yields similar results to the final chosen median solution (circled in red). Regions of interest for the metastatic lymph nodes were manually drawn over  $b_0$  dMRI images with the shortest diffusion time (100 ms) and then duplicated to other diffusion times. The metastatic nodes were used instead of the primary tumor because they are less sensitive to susceptibility artifacts and physiological involuntary motion, such as breathing and swallowing. According to KM (Eqs. 2 and 3) and as discussed previously, for the long-term regime, diffusivity is expected to be constant. To apply KM to voxels meeting these criteria, Eq. 5 was applied to voxels with the mean diffusivity between 0.5 and 1.5  $\mu\text{m}^2/\text{ms}$  and SD smaller than 15% of its mean, across all diffusion times.

## 3 | RESULTS

### 3.1 | Diffusion phantom

Figure 2A shows plots of diffusivity values across the different diffusion times for 0%, 10%, 20%, and 30% PVP concentrations vials, described for each of the three sites. As shown in the  $b_0$  images at 200 ms and 800 ms, 40% and 50% PVP concentration vials showed poor signal intensity close to the noise level due to their short  $T_1$  of 360 ms and 650 ms, respectively<sup>28</sup>; thus, they were not included in this study. The mean SNR (mean signal intensity/SD of background voxels) of  $b_0$  images with diffusion time = 800 ms are 243.7 (0% PVP), 212.7 (10% PVP), 148.8 (20% PVP), 73.1 (30% PVP), 17.6 (40% PVP), and 5.3 (50% PVP).

For the vials with 0%, 10%, 20%, and 30% PVP, the diffusivity difference measured had overall  $5.4 \pm 3.0\%$  deviation across the diffusion times from 200 ms to 800 ms (Figure 2A.):  $2.9 \pm 1.4\%$  for site 1,  $2.4 \pm 0.8\%$  for site 2, and  $5.4 \pm 3.0\%$  for site 3. Among the data from three sites, there are differences of  $5.8 \pm 2.6\%$  between sites 1 and 2,  $8.5 \pm 1.6\%$  between sites 1 and 3, and  $5.6 \pm 2.1\%$  between sites 2 and 3 (Figure 2A and Figure S2). The same differences are also observed among the data from SE-EPI data acquired within the same imaging sessions (Figure 2B and Figure S3), indicating that the differences are likely from the slightly different temperature of the phantom at three sites. Comparing the diffusivity values measured by the STEAM EPI with the values reported by the NIST (Figure 2A, green asterisks), the differences found for the longest diffusion time (800 ms) were  $9 \pm 3.1\%$  for site 1,  $3.5 \pm 1.8\%$  for site 2, and  $2.7 \pm 4.4\%$  for site 3. Additionally, regression analysis (Figure S4) and Bland-Altman plots

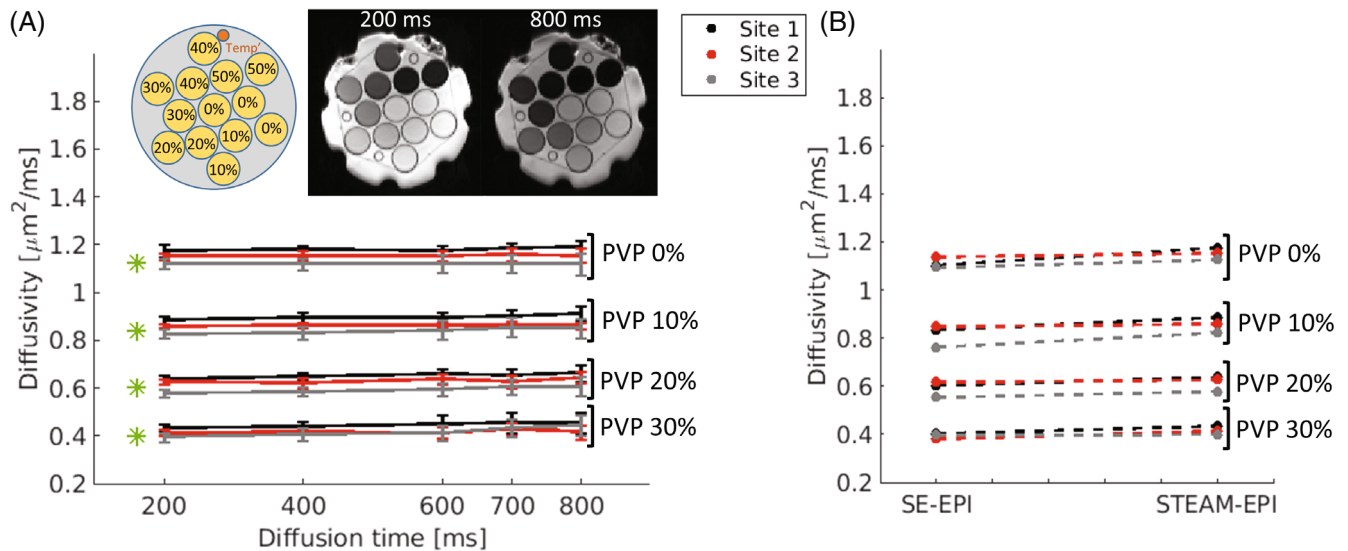


**FIGURE 2** Diffusivity measurements of National Institute of Standards and Technology (NIST) diffusion phantom at  $0^\circ\text{C}$ . A, Time-dependent experiments included multiple diffusion times ( $\Delta = 200, 400, 600, 700,$  and  $800$  ms) with same  $b$ -values up to 2000 for each diffusion time. Measurements were performed at three different 3T sites (see Methods section). Reported NIST diffusivity values are indicated by green asterisks. The phantom includes 13 vials of polymer concentration: 0%, 10%, 20%, 30%, 40%, and 50% polyvinylpyrrolidone (PVP; see the inset for the schematic diagram of the phantom). The STEAM-EPI  $b_0$  images at 200 ms and 800 ms show how signal varies as a function of PVP concentration. B, Measured diffusion values of spin-echo EPI (SE-EPI) versus STEAM-EPI with the shortest diffusion time of 200 ms. The plot values represent the average over the multiple vials, per concentration

(Figure S5) between the two show good correlations with a slight negative bias for sites 1 and 2.

$0$  ( $0.0 \pm 0.013$  and  $0.017 \pm 0.014$ , respectively) across the diffusion times.

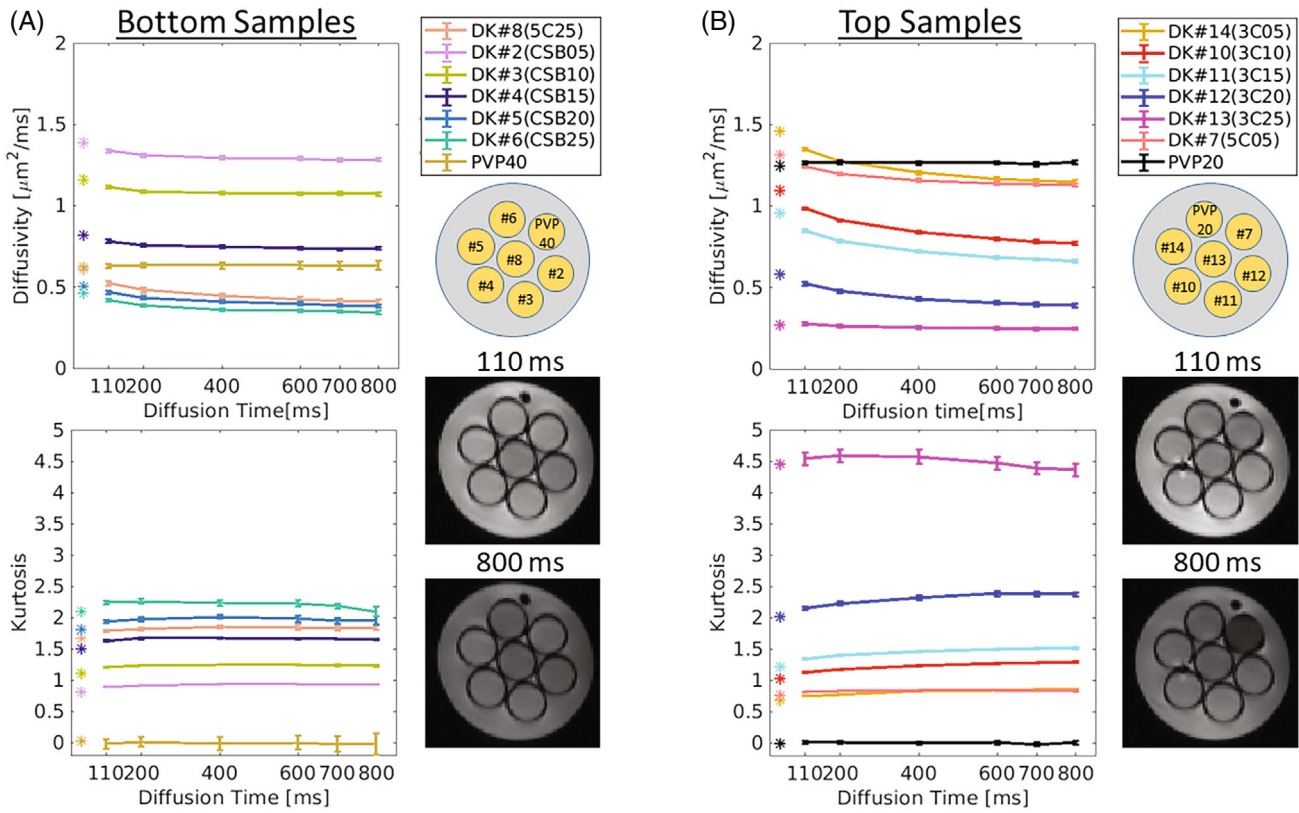
### 3.2 | Diffusion kurtosis imaging phantom

Figure 3 shows a summary of  $D(t)$  and  $K(t)$  measures from the DKI phantom. For the vials in the bottom layer (Figure 3A, indicated by CSB), diffusivity and kurtosis show low permeability characterized by weak dependency across the diffusion times, where  $D(t)$  decreases maximally by 27.8% (DK#8) from 110 ms to 800 ms, and  $K(t)$  increases maximally by 4.2% (DK#2). For the top layer (Figure 3B, indicated by C),  $D(t)$  and  $K(t)$  changes are more noticeable than in the CSB samples:  $D(t)$  decreases maximally by 34.3% (DK#12) from 110 ms to 800 ms, and  $K(t)$  increases maximally by 14.7% (DK#14). The C sample with 2.5% (DK#13, 3C25) shows that  $D(t)$  approaches a constant value in long diffusion times beyond 400 ms, where  $K(t)$  decreases monotonically (Figure S6). The diffusivity and kurtosis values measured by SE-EPI (Figure 3, indicated by asterisks at diffusion time  $\sim 45$  ms) are well in line with the trends of  $D(t)$  and  $K(t)$  measured by STEAM EPI (indicated by lines in Figure 3). Negative controls designated as PVP40 and PVP20 show  $D(t)$  approximately constant ( $0.63 \pm 0.002 \mu\text{m}^2/\text{ms}$  and  $1.27 \pm 0.004 \mu\text{m}^2/\text{ms}$ , respectively) and  $K(t)$  approximately

### 3.3 | Patients with head and neck cancer

Next, we tested time-dependent diffusion measurements in patients with head and neck cancer. Figure 4 shows  $b_0$  images, diffusivity, and kurtosis maps calculated from a patient with a metastatic cervical node measuring about  $27 \times 17$  mm. The images demonstrate good SNR and quality of diffusion-weighted images along with the estimated diffusivity and kurtosis maps for each diffusion time. For diffusion time of 700 ms, the signal intensity of the lymph node (marked by yellow arrow) remains high enough for estimation of diffusivity and kurtosis, compared with the surrounding tissue.

Figure 5A shows a representative case with a lymph node that has a cluster of voxels suitable for KM, based on the diffusivity and its SD over the diffusion times as described in the Methods section. For the two slices shown in Figure 5A, selected voxels were 47% and 35% of the whole lesion in each slice, respectively. The results of applying these criteria to select voxels suitable for KM in all 5 patients with head and neck cancer are shown in Figure 5B, where a higher variance is observed in diffusivity for the nonselected voxels than the variance for the selected voxels:  $D = (0.773 \pm 0.183, 0.769 \pm 0.186,$



**FIGURE 3** Diffusivity and kurtosis measurements of the diffusional kurtosis phantom. The phantom consists of two clusters of samples, bottom (A) and top (B), each composed of combinations of different chemical compositions (see Methods section). Time-dependent experiments included multiple diffusion times ( $\Delta = 110, 200, 400, 600, 700,$  and  $800$  ms) with the same  $b$ -values up to 2500 per diffusion time. Bottom and top clusters are characterized by their coded samples and their corresponding STEAM-EPI  $b_0$  images at 110 ms and 800 ms diffusion time. Measured SE-EPI diffusivity and kurtosis values are indicated by colored asterisks

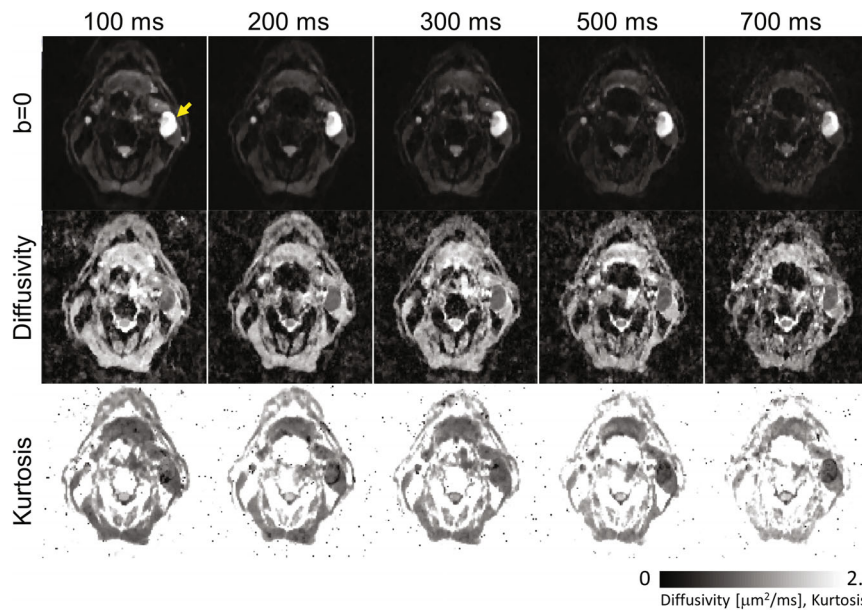


**FIGURE 4** Representative  $b_0$ , diffusivity, and kurtosis images acquired by time-dependent STEAM-EPI diffusion experiments of a 65-year-old patient with oropharyngeal squamous cell carcinoma and a metastatic left-sided cervical node (yellow arrow)

$0.782 \pm 0.189, 0.764 \pm 0.179, 0.764 \pm 0.178 \mu\text{m}^2/\text{ms}$ ) for diffusion times ( $t = 100, 200, 300, 500,$  and  $700$  ms) in the selected voxels; and  $D = (1.085 \pm 0.516, 1.065 \pm 0.487,$

$1.061 \pm 0.495, 1.045 \pm 0.515, 1.007 \pm 0.516 \mu\text{m}^2/\text{ms}$ ) for the nonselected voxels. Moreover,  $K(t)$  decreases gradually from the shortest diffusion time to the longest:

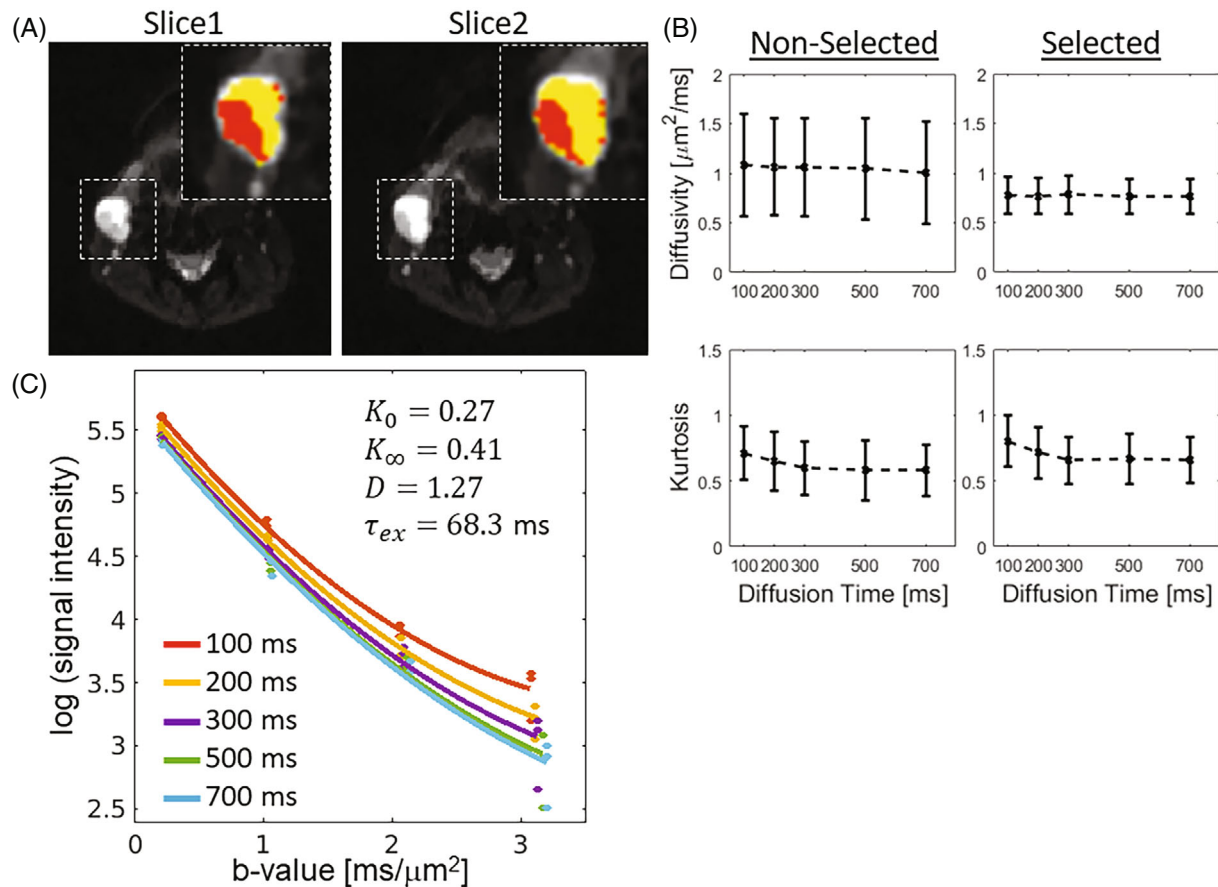


**FIGURE 5** Voxel selection for data analysis using the Kärger model (KM). A, A metastasis lesion shown in two slices of a 50-year-old patient with oropharyngeal squamous cell carcinoma. The voxels in the metastatic lymph node (noted by the dashed box) are divided into nonselected (yellow) and selected tumor voxels (red) based on the variability of  $D(t)$  (see Methods section). B, Diffusivity and kurtosis values calculated from the nonselected and selected voxels of the 5 patients with head and neck cancer with lymph metastasis lesions. C, A representative voxel-wise signal (taken from the selected region) is plotted as a function of  $b$ -value for all five diffusion times

$0.803 \pm 0.194$  to  $0.66 \pm 0.176$  for the selected voxels, and  $0.712 \pm 0.204$  to  $0.582 \pm 0.197$  for the nonselected voxels. Additionally, a representative voxel signal taken from the selected region was plotted as a function of  $b$ -value (Figure 5C) for all five diffusion times together with their corresponding fits.

Figure 6 shows representative parameter maps of 5 patients with KM analysis applied to the selected voxels. Among the 5 patients,  $72\% \pm 23\%$  of all voxels within the lymph nodes regions of interest were selected for KM analysis according to the  $D(t)$  trend. For comparison, Figure S7 shows the KM parameter maps of all voxels regardless of the selection step. The median  $K_0$ , the magnitude of  $K(t)$  decay, is between 0.3 and 0.65. The median cellular-interstitial exchange time  $\tau_{ex}$  is between 58.5 ms and 70.6 ms. The KM analysis results of the selected voxels in all five cases are summarized in Table 1 and Figure 7. To examine the potential difference between  $T_1$  values of the intracellular and extracellular compartments, we show a voxel-wise linear model fit of a representative

lymph node, demonstrating a mono-exponential decay (Figure S8). Finally, the upper  $b$ -value limit ( $b < 3/(DK)$ ) as defined in the Theory section, yielded that, for a representative case (including all slices), 73.7% of all pixels included the highest  $b$ -value (ie,  $3000 \text{ s/mm}^2$ ), while 26.1% included  $b$ -value =  $2000 \text{ s/mm}^2$  and  $< 1\%$  below that.

## 4 | DISCUSSION

In many biological tissues, and specifically in cancer lesions, the highly heterogeneous tissue microstructure and variable permeability can lead to non-Gaussian and time-dependent water diffusion.<sup>36</sup> To examine this phenomenon, we explored time-dependent diffusion and kurtosis measurements in phantoms and in head and neck cancer using an in-house STEAM-EPI pulse sequence with a range of relatively long diffusion times. We found that the phantom data support that the STEAM-EPI sequence



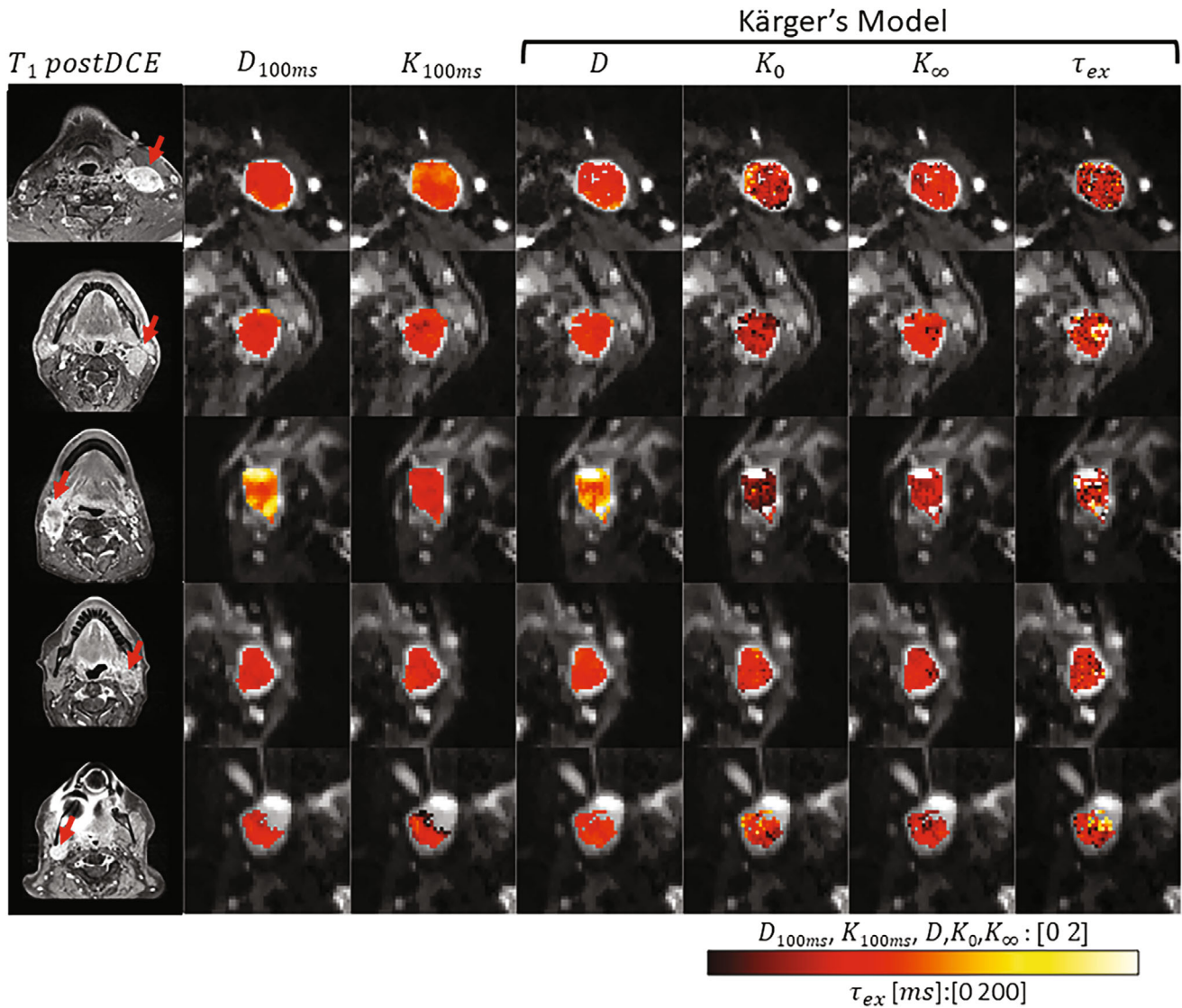


**FIGURE 6** Parametric maps as calculated by KM for the selected voxels of the 5 patients included in the study. Diffusivity ( $D$ ) and kurtosis ( $K$ ) maps with 100-ms diffusion time were calculated by a weighted linear least-squares fit method. Diffusivity ( $D$ ),  $K_0$ ,  $K_\infty$ , and  $\tau_{ex}$  maps were calculated by KM

**TABLE 1** Summary of KM parameters of the metastatic lymph nodes of all 5 patients

	$D$	$K_0$	$K_\infty$	$\tau_{ex}$
Case 1	0.76 [0.69 0.86]	0.65 [0.40 0.87]	0.75 [0.61 0.88]	66.87 [49.60 84.15]
Case 2	0.85 [0.80 0.89]	0.46 [0.33 0.59]	0.81 [0.72 0.88]	63.71 [49.96 82.72]
Case 3	1.15 [0.99 1.28]	0.3 [0.21 0.40]	0.61 [0.51 0.68]	58.47 [43.54 79.04]
Case 4	0.87 [0.82 0.92]	0.61 [0.47 0.73]	0.69 [0.60 0.77]	70.57 [57.15 85.64]
Case 5	0.92 [0.85 0.97]	0.48 [0.33 0.69]	0.72 [0.60 0.81]	63.05 [48.60 80.25]

Note: The values are presented as the median [25th and 75th percentiles] from the selected voxels in all slices of each lymph node of individual patients. The diffusional parameter is in  $\mu\text{m}^2/\text{ms}$  units and exchange time in milliseconds.

can be used reliably to measure diffusivity and diffusional kurtosis<sup>14</sup> for a constant b-value experiment over diffusion times ranging from 100 ms to 800 ms. Our study

results also suggest that the cellular-interstitial water exchange time can be measured using a biophysical modeling approach known as the Kärger model.<sup>27</sup>

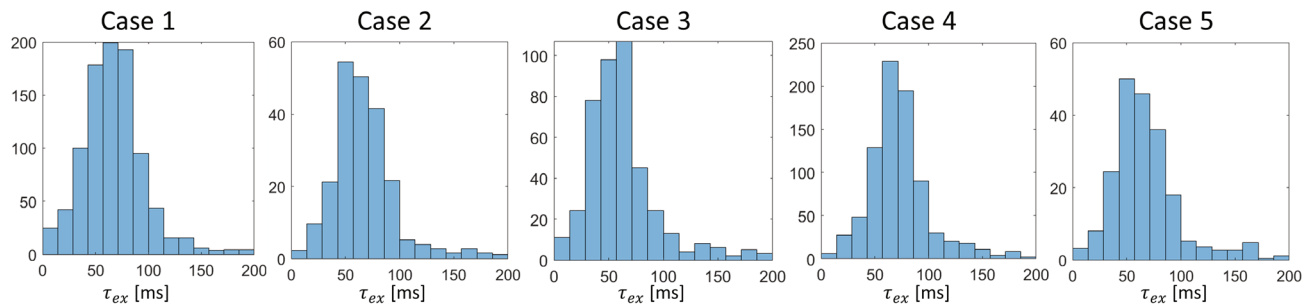


FIGURE 7 Histograms of  $\tau_{ex}$  values for all 5 head and neck patients

## 4.1 | Phantoms

Diffusion phantoms are used for validation of diffusion acquisition and analysis methods and serve as a good quality control tool.<sup>37</sup> In this study, we used an established NIST diffusion phantom<sup>28</sup> to perform time-dependent diffusion measurements by STEAM-EPI acquisition. To assess the reproducibility of our STEAM-EPI method, we repeated the measurements across three MRI 3T systems at two imaging centers. Our results suggest that diffusion time does not affect diffusivity values of the phantoms at near 0°C. It was further confirmed by comparing them with the results measured by the conventional SE-EPI method acquired with much shorter diffusion times (~50 ms). We also show that our results agree with the reported diffusivity values from NIST.<sup>28</sup> All of these test results confirm that the diffusion weighting applied at the range of long diffusion times is accurately accounted for calculation of the b-matrices that are used for estimation of diffusivities and kurtosis for the corresponding diffusion times.

The comparison of diffusivity values measured at three sites showed a small, but noticeable difference among the sites (Figure 2) in the data collected using both our in-house STEAM-EPI and the vendor-provided SE-EPI sequences. The phantom was filled with ice water until it reached 0°C; however, temperature was not consistently monitored during scans. Hence, we assume that some discrepancy can arise from differences in the actual temperature inside the phantom, which apparently relates to temperature drift. In addition, we cannot rule out any potential differences in the performances of the gradient systems, phantom positioning off isocenter and gradient rise times, which could also affect the accuracy of the diffusivity measurement among the three sites. These discrepancies can occur between sites but also during the experiment itself. In our study, since the different diffusion times were acquired in ascending order, we observed a slight increase in diffusivity between the shortest and the longest diffusion (5.1% for site 1, 2.81% for site 2, and 10.5% for site 3), which can imply an increase in temperature

over time. At any rate, our observations in this study substantiate that, with careful control and monitoring of the temperature of the phantom during the scan, this type of diffusion phantom can be used to assess any changes in the hardware and/or software. This is consistent with the negative control measurements for DKI phantom performed at equilibrium room temperature.

We also examined a novel DKI phantom that provides realistic diffusional kurtosis values in a physiologically plausible range.<sup>29</sup> This new generation DKI phantom consists of nanoscopic vesicles made with a combination of alcohols and surfactants. Using the DKI phantom, time-dependent diffusion experiments were performed to measure both diffusion and kurtosis. In principle, the high molecular weight alcohol samples, characterized by impenetrable barrier, are not expected to show exchange. Looking closer at a few of the samples found in Figure S6, diffusivity of the lower concentration (mixture of and cetyltrimethyl ammonium bromide, indicated by C) showed gradual decrease in diffusion and increase in kurtosis, which implies an impermeable membrane or a short diffusion regime (Figure S6A). For the 2.5% concentration (Figure S6B), diffusivity initially shows a gradual decrease for the short diffusion times and then approaches to a constant diffusivity value for the long diffusion times (> 400 ms). Interestingly, for the same long diffusion times, kurtosis shows a monotonically decrease, rather similar to what is expected in the Karger regime with long diffusion times. The exchange time estimated from the time course is 102 ms. One possible explanation for these exchange properties is the mixture of ceteryl alcohol and cetyltrimethyl ammonium bromide, which have long-chain alcohols and likely have some “intermediate” vesicle permeability. Nevertheless, this observation requires further investigation of the material chemical properties with improved precision, which could also be extended to make a phantom with different exchange times. Further characterization of cross-scanner reproducibility would require temperature calibration of the DKI phantom (ongoing) to rule out contribution of different scanner room environment temperatures.<sup>26</sup> Finally,

please note that due to the temperature difference between the DKI phantom (room temperature) and the NIST phantom ( $\sim 0^\circ\text{C}$ ) and its potential effect on  $T_1$  relaxation timing, we had sufficient signal in the DKI phantom to include the PVP40 data.<sup>38</sup>

## 4.2 | Patients with head and neck cancer

Cellular-interstitial water exchange time has been suggested to be associated with a number of important cellular properties such as membrane permeability, tumor aggressiveness,<sup>39</sup> and treatment response.<sup>23</sup> Being able to measure water exchange can help understanding some of its mechanisms governed primarily by molecule diffusivity across the plasma membrane and transport via aquaporins.<sup>40</sup> Moreover, it was shown that cancer cells with increased metabolic activity can be associated with higher water exchange rates compared with normal tissues.<sup>22</sup> Here, we examine the use of KM for measuring water exchange time in head and neck cancer without an exogenous contrast agent. To achieve the long-term diffusion regime where diffusivity is expected to be constant, we have selected voxels that meet these criteria. As a result, only a portion of the whole metastasis lymph node was selected (Figure 5), experiencing significant ( $p = 2.2\text{e-}06$ ) lower diffusivity variance compared with the nonselected voxels. This difference stems from the KM criteria defined in the Methods section. In Figure S7, we show additional parametric maps that were analyzed for the whole lesion without selecting voxels. Overall, the constant diffusivity and water exchange time exhibited in this study can reflect many possible microstructural arrangements between intracellular and extracellular compartments. However, our present study was not designed to specifically probe other microstructural properties, such as cell size and extracellular volume fraction, which would require having much shorter diffusion times as shown in our earlier study.<sup>11</sup> For the voxels that do not meet the criteria for KM, future study is warranted to explore the options of using other biophysical models, including the random permeable barrier model<sup>41</sup> or Mitra model.<sup>42</sup>

The median exchange times measured in this study ranged between 58.5 ms and 70.6 ms. These values are similar to the exchange times reported in perfused glial cells measured by NMR<sup>43</sup> and are slightly lower than the ones recently reported for two breast cancers (70 ms and 106 ms).<sup>20</sup> Because the time to diffuse across a cancer cell with a radius of 4  $\mu\text{m}$  and diffusivity of approximately 1.5  $\mu\text{m}^2/\text{ms}$  is 10 ms, these water exchange times from our study and previous studies indicate that the exchange is barrier-limited, meaning that the estimated

exchange times exceed the characteristic time.<sup>19,20</sup> To date, only a limited number of studies have used time-dependent diffusion experiments to measure water exchange times in tumors. Most studies have measured the intracellular water lifetime parameter ( $\tau_i = \tau_{\text{ex}}/v_e$ ) using DCE MRI.<sup>21,23</sup> In head and neck cancer DCE studies, the exchange values estimated from the intracellular water lifetime and extracellular volume fraction are  $71 \pm 33$  ms for metastatic lymph nodes<sup>44</sup> and 96 ms and 107 ms for cancer patients with partial and complete response, respectively.<sup>45</sup> These exchange times are close to those measured using the KM in our present study. To date, there is no histological method to measure water exchange time, and no in vivo imaging method has been established as a gold-standard method. The main advantage of using the proposed time-dependent diffusion experiment is the fact that, unlike DCE, dMRI does not require contrast injection.

This study had several limitations. Optimization of the diffusion MRI protocol was not within the scope of this proof-of-concept study. The diffusion times used in this study were arbitrary selected over the range between 100 ms and 700 ms. Future studies need to be conducted to determine optimal combinations of diffusion times and  $b$ -values for robust estimation of diffusion and KM parameters, including water exchange time. Moreover, as KM solutions for  $D$  and  $K(t)$  apply under the narrow pulse assumption,<sup>46</sup> future studies should restrict diffusion gradient duration as short as possible. Additionally, since STEAM EPI is heavily dependent on effective spoiler gradients, in charge of crushing residual magnetization after storage, some consideration in the choice of  $b$ -values is needed in order to avoid the possibility that spoiler gradients become stronger than the diffusion gradients, which may lead to slightly shortening effect in diffusion timing. Another limitation is a small number of patients included in the study. A follow-up study with a larger cohort will further strengthen the finding and confirm the feasibility of using KM to measure water exchange time. Moreover, our study did not include repeatability measures over the same patient, which could further strengthen the findings presented in this study. Future study is warranted to include repeatability measures on the same patient in one site.<sup>47</sup> Finally, from plotting the  $b_0$  signal of a representative lymph node as a function of mixing time (Figure S8), we observed that the  $T_1$  recovery is mono-exponential. This suggests that the potential difference between  $T_1$  values of the intracellular and extracellular compartments is negligible. However, future study is warranted to investigate more in depth the potential influence of  $T_1$  in the cellular-interstitial water exchange among patients with head and neck cancer.


## 5 | CONCLUSIONS


In this study we investigated the reliability of measuring water exchange times based on diffusivity and diffusional kurtosis at long diffusion times using a stimulated-echo DWI. We used two well-established diffusion phantoms and found that diffusion and kurtosis show stable values over a wide range of diffusion times. In patients with head and neck cancer, we found that the Kärger model is a valid model for measuring water exchange time in a large portion ( $72 \pm 23\%$ ) of metastasis lymph node voxels.


## FUNDING INFORMATION


National Institute of Health; Grant/Award Nos. UH3CA228699, R01CA160620, R01CA219964, and R01EB028774

## ORCID

Eddy Solomon  <https://orcid.org/0000-0001-9204-4518>

Gregory Lemberskiy  <https://orcid.org/0000-0002-8336-7486>

Stephen E. Russek  <https://orcid.org/0000-0002-8788-2442>

Sunghoon Gene Kim  <https://orcid.org/0000-0002-6288-0678>

## REFERENCES

- Chenevert TL, McKeever PE, Ross BD. Monitoring early response of experimental brain tumors to therapy using diffusion magnetic resonance imaging. *Clin Cancer Res*. 1997;3:1457-1466.
- Galons JP, Altbach MI, Paine-Murrieta GD, Taylor CW, Gillies RJ. Early increases in breast tumor xenograft water mobility in response to paclitaxel therapy detected by non-invasive diffusion magnetic resonance imaging. *Neoplasia*. 1999;1:113-117.
- Moffat BA, Chenevert TL, Lawrence TS, et al. Functional diffusion map: a noninvasive MRI biomarker for early stratification of clinical brain tumor response. *Proc Natl Acad Sci USA*. 2005;102:5524-5529.
- Chinnaiyan AM, Prasad U, Shankar S, et al. Combined effect of tumor necrosis factor-related apoptosis-inducing ligand and ionizing radiation in breast cancer therapy. *Proc Natl Acad Sci USA*. 2000;97:1754-1759.
- Costantini M, Belli P, Rinaldi P, et al. Diffusion-weighted imaging in breast cancer: relationship between apparent diffusion coefficient and tumour aggressiveness. *Clin Radiol*. 2010;65:1005-1012.
- Solomon E, Liberman G, Nissan N, Furman-Haran E, Sklair-Levy M, Frydman L. Diffusion-weighted breast MRI of malignancies with submillimeter resolution and immunity to artifacts by spatiotemporal encoding at 3T. *Magn Reson Med*. 2020;84:1391-1403.
- Gupta RK, Cloughesy TF, Sinha U, et al. Relationships between choline magnetic resonance spectroscopy, apparent diffusion coefficient and quantitative histopathology in human glioma. *J Neurooncol*. 2000;50:215-226.
- Kim S, Chi-Fishman G, Barnett AS, Pierpaoli C. Dependence on diffusion time of apparent diffusion tensor of ex vivo calf tongue and heart. *Magn Reson Med*. 2005;54:1387-1396.
- Lemberskiy G, Rosenkrantz AB, Veraart J, Taneja SS, Novikov DS, Fieremans E. Time-dependent diffusion in prostate cancer. *Invest Radiol*. 2017;52:405-411.
- Novikov DS, Jensen JH, Helpert JA, Fieremans E. Revealing mesoscopic structural universality with diffusion. *Proc Natl Acad Sci USA*. 2014;111:5088-5093.
- Reynaud O, Winters KV, Hoang DM, Wadghiri YZ, Novikov DS, Kim SG. Pulsed and oscillating gradient MRI for assessment of cell size and extracellular space (POMACE) in mouse gliomas. *NMR Biomed*. 2016;29:1350-1363.
- Reynaud O, Winters KV, Hoang DM, Wadghiri YZ, Novikov DS, Kim SG. Surface-to-volume ratio mapping of tumor microstructure using oscillating gradient diffusion weighted imaging. *Magn Reson Med*. 2016;76:237-247.
- Jansen JF, Stambuk HE, Koutcher JA, Shukla-Dave A. Non-Gaussian analysis of diffusion-weighted MR imaging in head and neck squamous cell carcinoma: a feasibility study. *AJNR Am J Neuroradiol*. 2010;31:741-748.
- Jensen JH, Helpert JA, Ramani A, Lu H, Kaczynski K. Diffusional kurtosis imaging: the quantification of non-gaussian water diffusion by means of magnetic resonance imaging. *Magn Reson Med*. 2005;53:1432-1440.
- Kiselev VG, Il'yasov KA. Is the "biexponential diffusion" biexponential? *Magn Reson Med*. 2007;57:464-469.
- Goshima S, Kanematsu M, Noda Y, Kondo H, Watanabe H, Bae KT. Diffusion kurtosis imaging to assess response to treatment in hypervascular hepatocellular carcinoma. *AJR Am J Roentgenol*. 2015;204:W543-W549.
- Kim S, Loevner L, Quon H, et al. Diffusion-weighted magnetic resonance imaging for predicting and detecting early response to chemoradiation therapy of squamous cell carcinomas of the head and neck. *Clin Cancer Res*. 2009;15:986-994.
- Jespersen SN, Olesen JL, Hansen B, Shemesh N. Diffusion time dependence of microstructural parameters in fixed spinal cord. *Neuroimage*. 2018;182:329-342.
- Fieremans E, Novikov DS, Jensen JH, Helpert JA. Monte Carlo study of a two-compartment exchange model of diffusion. *NMR Biomed*. 2010;23:711-724.
- Zhang J, Lemberskiy G, Moy L, Fieremans E, Novikov DS, Kim SG. Measurement of cellular-interstitial water exchange time in tumors based on diffusion-time-dependent diffusional kurtosis imaging. *NMR Biomed*. 2021;34:e4496.
- Springer CS, Jr, Li X, Tudorica LA, et al. Intratumor mapping of intracellular water lifetime: metabolic images of breast cancer? *NMR Biomed*. 2014;27:760-73.
- Lowry M, Zelfhof B, Liney GP, Gibbs P, Pickles MD, Turnbull LW. Analysis of prostate DCE-MRI: comparison of fast exchange limit and fast exchange regimen pharmacokinetic models in the discrimination of malignant from normal tissue. *Invest Radiol*. 2009;44:577-584.
- Chawla S, Loevner LA, Kim SG, et al. Dynamic contrast-enhanced MRI-derived intracellular water lifetime ( $\tau_i$ ): a prognostic marker for patients with head and neck squamous cell carcinomas. *Am J Neuroradiol*. 2018;39:138-144.
- Sigmund EE, Novikov DS, Sui D, et al. Time-dependent diffusion in skeletal muscle with the random permeable barrier model (RPBM): application to normal controls and chronic

- exertional compartment syndrome patients. *NMR Biomed.* 2014;27:519-528.
25. Novikov DS, Kiselev VG. Effective medium theory of a diffusion-weighted signal. *NMR Biomed.* 2010;23:682-697.
  26. Novikov DS, Fieremans E, Jespersen SN, Kiselev VG. Quantifying brain microstructure with diffusion MRI: theory and parameter estimation. *NMR Biomed.* 2019;32:e3998.
  27. Karger J. NMR self-diffusion studies in heterogeneous systems. *Adv Colloid Interface Sci.* 1985;23:129-148.
  28. Russek SE. NIST/NIBIB medical imaging phantom lending library. *National Institute of Standards and Technology.* 2021.
  29. Malyarenko DI, Swanson SD, Konar AS, et al. Multicenter repeatability study of a novel quantitative diffusion kurtosis imaging phantom. *Tomography.* 2019;5:36-43.
  30. Veraart J, Novikov DS, Christiaens D, Ades-Aron B, Sijbers J, Fieremans E. Denoising of diffusion MRI using random matrix theory. *Neuroimage.* 2016;142:384-396.
  31. Kellner E, Dhital B, Kiselev VG, Reiser M. Gibbs-ringing artifact removal based on local subvoxel-shifts. *Magn Reson Med.* 2016;76:1574-1581.
  32. Veraart J, Fieremans E, Novikov DS. Diffusion MRI noise mapping using random matrix theory. *Magn Reson Med.* 2016;76:1582-1593.
  33. Andersson JLR, Sotiropoulos SN. An integrated approach to correction for off-resonance effects and subject movement in diffusion MR imaging. *Neuroimage.* 2016;125:1063-1078.
  34. Buades A, Coll B, Morel JM. A non-local algorithm for image denoising. In: Proceedings of the IEEE Computer Society Conference on Computer Vision and Pattern Recognition, San Diego, California, USA, 2005. pp. 60-5.
  35. Veraart J, Sijbers J, Sunaert S, Leemans A, Jeurissen B. Weighted linear least squares estimation of diffusion MRI parameters: strengths, limitations, and pitfalls. *Neuroimage.* 2013;81:335-346.
  36. Jensen JH, Helpert JA. MRI quantification of non-Gaussian water diffusion by kurtosis analysis. *NMR Biomed.* 2010;23:698-710.
  37. Keenan KE, Ainslie M, Barker AJ, et al. Quantitative magnetic resonance imaging phantoms: a review and the need for a system phantom. *Magn Reson Med.* 2018;79:48-61.
  38. Statton BK, Smith J, Finnegan ME, Koerzdoerfer G, Quest RA, Grech-Sollars M. Temperature dependence, accuracy, and repeatability of T1 and T2 relaxation times for the ISMRM/NIST system phantom measured using MR fingerprinting. *Magn Reson Med.* 2022;87:1446-1460.
  39. Li X, Huang W, Morris EA, et al. Dynamic NMR effects in breast cancer dynamic-contrast-enhanced MRI. *Proc Natl Acad Sci USA.* 2008;105:17937-17942.
  40. Agre P, Bonhivers M, Borgnia MJ. The aquaporins, blueprints for cellular plumbing systems. *J Biol Chem.* 1998;273:14659-14662.
  41. Novikov DS, Fieremans E, Jensen JH, Helpert JA. Random walks with barriers. *Nat Phys.* 2011;7:508-514.
  42. Mitra PP, Sen PN, Schwartz LM. Short-time behavior of the diffusion-coefficient as a geometrical probe of porous-media. *Phys Rev B.* 1993;47:8565-8574.
  43. Pfeuffer J, Flögel U, Leibfritz D. Monitoring of cell volume and water exchange time in perfused cells by diffusion-weighted <sup>1</sup>H NMR spectroscopy. *NMR Biomed.* 1998;11:11-18.
  44. Kim S, Quon H, Loevner LA, et al. Transcytolemmal water exchange in pharmacokinetic analysis of dynamic contrast-enhanced MRI data in squamous cell carcinoma of the head and neck. *J Magn Reson Imaging.* 2007;26:1607-1617.
  45. Kim S, Loevner LA, Quon H, et al. Prediction of response to chemoradiation therapy in squamous cell carcinomas of the head and neck using dynamic contrast-enhanced MR imaging. *Am J Neuroradiol.* 2010;31:262-268.
  46. Li JR, Nguyen HT, Nguyen DV, Haddar H, Coatleven J, Le Bihan D. Numerical study of a macroscopic finite pulse model of the diffusion MRI signal. *J Magn Reson.* 2014;248:54-65.
  47. O'Connor JP, Aboagye EO, Adams JE, et al. Imaging biomarker roadmap for cancer studies. *Nat Rev Clin Oncol.* 2017;14:169-186.

## SUPPORTING INFORMATION

Additional supporting information may be found in the online version of the article at the publisher's website.

**FIGURE S1** Example of Kärger's model estimates ( $D, K_0, \tau_{ex}, K_\infty$ ), as measured by Eq. 5, along with final chosen median solution (circled in red)

**FIGURE S2** Diffusivity measurements of the National Institute of Standards and Technology (NIST) diffusion phantom for 0%, 10%, 20%, and 30% polyvinylpyrrolidone (PVP), combined across all diffusion times

**FIGURE S3** SE-EPI Regression analysis ( $R^2$  and slope) between diffusivity values measured by STEAM EPI with shortest diffusion time (200 ms) and stimulated-echo EPI of the NIST diffusion phantom. The analysis includes diffusivity measurements of the NIST diffusion phantom for 0%, 10%, 20%, and 30% PVP, for three different 3T sites

**FIGURE S4** Regression analysis ( $R^2$  and slope) between diffusivity values measured by STEAM EPI and diffusivity values as reported by NIST. The analysis includes diffusivity measurements of the NIST diffusion phantom for 0%, 10%, 20%, and 30% PVP

**FIGURE S5** Bland-Altman plots between diffusivity values measured by STEAM EPI and diffusivity values as reported by NIST. The analysis includes diffusivity measurements of the NIST diffusion phantom for 0%, 10%, 20%, and 30% PVP

**FIGURE S6** A, Representative samples of the diffusional kurtosis imaging (DKI) phantom that shows similar trend of gradual decrease of  $D$  and increase of  $K$ . B, One sample (DK#13) shows a distinct pattern of  $K$  that initially increases while  $D$  decreases for relatively short diffusion

times. This trend is followed by a much slower change in  $D$  with a decreasing pattern of  $K$ , for relatively long diffusion times. This is similar to the short and long diffusion regime behaviors expected according to the Kärger model considered in this study

**FIGURE S7** Representative parametric maps of the Kärger model of the whole lesion voxels versus selected voxels. Diffusion ( $D$ ) and kurtosis ( $K$ ) maps with 100 ms diffusion time were calculated by a weighted linear least-square fit method. Diffusion ( $D$ ),  $K_0$ ,  $K \infty$ , and  $\tau_{\text{ex}}$  were calculated by the Kärger model

**FIGURE S8** Voxel-wise linear model fit of  $b_0$  signal in the logarithmic scale of a metastatic lymph node with estimated  $R^2$  and  $T_1$  relaxation timing

**How to cite this article:** Solomon E, Lemberskiy G, Baete S, et al. Time-dependent diffusivity and kurtosis in phantoms and patients with head and neck cancer. *Magn Reson Med.* 2023;89:522-535. doi: 10.1002/mrm.29457